designs

MDPI

Article

Performance Analysis of Two Receiver Arrangements for Wireless Battery Charging System

Abhay Kumar [1,*], Rupesh Kumar Jha [2], Manuele Bertoluzzo [1,*], Chetan B. Khadse [3], Swati Jaiswal [4], Gourang Mulay [5] and Amritansh Sagar [1]

[1] Department of Industrial Engineering, University of Padova, 35131 Padua, Italy
[2] Tata Consultancy Services, Banglore 560066, India
[3] School of Electrical Engineering, Dr. Vishwanath Karad MIT World Peace University, Pune 411038, India
[4] Computer Engineering Department, Pimpri Chinchwad College of Engineering, Pune 411044, India
[5] School of Electrical and Communication Engineering, Dr. Vishwanath Karad MIT World Peace University, Pune 411038, India
* Correspondence: abhay.kumar@studenti.unipd.it (A.K.); manuele.bertoluzzo@unipd.it (M.B.)

Abstract: Two different arrangements for Wireless Battery Charging Systems (WBCSs) with a series-parallel resonant topology have been analyzed in this paper. The first arrangement charges the battery by controlling the receiver-side rectifier current and voltage without a chopper, while the second arrangement charges it with a chopper while keeping the chopper input voltage constant. The comparison of these two arrangements is made based on their performance on various figures of merit, such as the sizing factor of both the supply voltage source and receiver coil, overall system efficiency, power-transfer ratio, receiver efficiency, and cost estimation. Later, the simulated study is verified by the experimental setup designed to charge the electric vehicle.

Keywords: EV battery charging; wireless charging; charging topologies

Citation: Kumar, A.; Jha, R.K.; Bertoluzzo, M.; Khadse, C.B.; Jaiswal, S.; Mulay, G.; Sagar, A. Performance Analysis of Two Receiver Arrangements for Wireless Battery Charging System. *Designs* **2023**, *7*, 92. https://doi.org/10.3390/designs7040092

Academic Editors: Quanqing Yu and Pawan Sharma

Received: 2 April 2023
Revised: 30 June 2023
Accepted: 4 July 2023
Published: 6 July 2023

1. Introduction

The motivation for adopting a vehicle powered by a clean source of energy is to reduce polluting emissions due to the transportation facility [1,2]. Emerging technology, such as Wireless Battery Charging (WBC), enables the transfer of power to the vehicle without a wired connection [3]. Other advantages associated with WBC systems are (i) the absence of plug, cable, and outlet, (ii) the easy charging process, (iii) the mitigation of any shock during bad weather conditions, and many more. In view of this, this technology is the emerging technology for Electrical Vehicle (EV) charging [4–7].

The block diagram of WBC systems is presented in Figure 1. As shown, the transmitter and receiver are the two major stages, consisting of power converters, a resonant circuit, and coupling coils. The coils at both stages are coupled inductively and have an air gap from 15 to 20 cm.

The power converter in the transmitter stage includes a Power Factor Correction circuit (PFC) and a High-Frequency Inverter (HFI). The role of the PFC is to convert grid voltage into dc voltage while maintaining power factor unity, and HFI converts this dc voltage into ac voltage at a high frequency suitable for the WBC system, whose output voltage magnitude can be controlled by the phase shift technique. In the receiver stage, the power converter converts the ac voltage induced in the receiver coil into the dc voltage needed to charge the EV battery.

For better efficiency and smaller power supply sizing, the WBC system employs the Compensation Network (CN) along with its coupling coil [8,9]. In the simplest arrangements, the CN is a capacitor connected to the coils that resonates with the coil inductance at the supply frequency. Depending upon the different combinations of the coils, there

are four fundamental topologies possible, such as series–series (SS), series–parallel (SP), parallel–series (PS), and parallel–parallel (PP) [10–18].

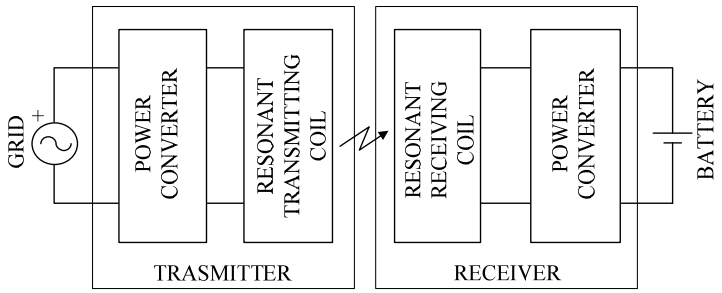

Figure 1. WBC systems schematics.

Different architectures are proposed for receiver power circuitry together with parallel compensation [19,20] proposed, where the power conversion circuitry of the receiver includes a diode rectifier to supply the load with a direct voltage and resorts to different solutions for the adjustment of the voltage amplitude; research [21,22] provide the control of the AC voltage before applying it to the diode rectifier for secondary parallel compensation; and [23–25] use a diode rectifier cascaded by a buck converter. The most popular technique for a WBC receiver is to charge the battery in a straightforward manner with the diode rectifier or through a chopper and control the voltage of the power source in the transmitter to adjust the power absorbed by the battery. Based on the abovementioned different charging arrangements, this paper compares two types of arrangements, referred to here as arrangements #1 and #2, respectively. Arrangement #1 charges the battery without the control rectifier current/voltage, while Arrangement #2 charges the battery with the chopper, keeping its input voltage constant. The paper performs this analysis considering the SP compensation topology and cost estimation.

The paper is organized as follows: Section 2 briefly describes the operation of a battery-charging process and finds some basic equations for SP topology. Section 3 introduces and determines FOMs (figures of merit) for the SP topology. Section 4 examines the operation of both arrangements. Section 5 discusses the effect of the amplitude of the chopper input voltage on FOMs. Section 6 include the experimental details and results. Section 7 concludes the paper.

Throughout the paper, upper-case symbols with a superimposed bar represent the phasor relevant to the sinusoidal quantities, and their rms value is represented by an upper-case symbol.

2. WBC Background

2.1. Battery Charging

Figure 2 shows the two sequential modes of EV battery charging, such as Constant Current (CC) and Constant Voltage (CV). Here, I_B, V_B, R_B, and P_B are assigned for battery current, voltage, resistance, and power, respectively. Battery resistance is defined as the ratio of battery voltage and current. Along with this, I_{co} and V_{co} are the cutoff current and voltage, and N is the point of transition from CC to CV mode. For the sake of keeping the study simple, an assumption is made that the battery voltage in CC mode is in a linear charging profile. All the parameters in Figure 2, such as current, voltage, resistance, and power, are normalized. The normalization is carried out as follows: (i) current is normalized to the CC mode current I_{CC}; (ii) voltage is normalized to the maximum battery voltage V_M; (iii) resistance is normalized to the resistance at point N, equal to the ratio of V_M and I_{CC} and is denoted by R_N; and (iv) power is normalized to the power at point N, given by the product of V_M and I_{CC} and is denoted as P_N. It is observed that the battery resistance in CC mode increased from R_I, which is the ratio of voltage and current at the beginning of CC mode, to R_F, which is the ratio of V_M and I_{CO} through R_N. Also, battery power increases

from P_I to P_N and then decreases to P_F. Resistance R_B as a function of P_B, in CC and CV modes, is represented as

$$R_B = \frac{1}{I_{CC}^2} P_B,\ R_B = V_M^2 \frac{1}{P_B} \tag{1}$$

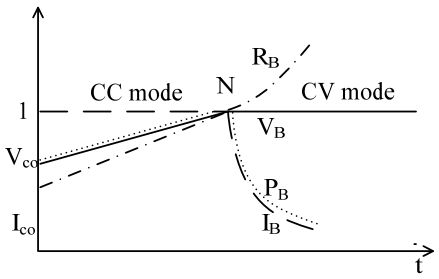

Figure 2. Battery-charging profile: normalized voltage as in solid line, normalized current as in dashed line, normalized power as in dotted line, and normalized resistance as in dashed-dotted line.

2.2. Analysis of SP Topology

Figure 3 shows the series–parallel topology for the WBC system. The symbols in Figure 3 are assigned as follows: (i) $\overline{V}_S$ is the power source voltage; (ii) $\overline{I}_T$ and $\overline{I}_R$ are the transmitter and receiver side currents; (iii) C_T and C_R are the transmitter and receiver resonant capacitors; (iv) $\overline{V}_{Tt}$ and $\overline{V}_{Rt}$ are the transmitter and receiver coils terminal voltages; (v) L_T and L_R are the transmitter and receiver coils inductances; (vi) r_T and r_R are the transmitter and receiver coils parasitic resistances; (vii) $\overline{V}_T$ and $\overline{V}_R$ are the voltage induced in the transmitter and receiver coils due to the effect of mutual inductance; (viii) $\overline{I}_C$ and $\overline{I}_L$ are the receiver-side capacitor current and load current; and (ix) R_L and $\overline{V}_L$ are the load resistance and voltage across R_L. The induced voltages $\overline{V}_T$ and $\overline{V}_R$ are given by

$$\begin{aligned} \overline{V}_T &= j\omega M \overline{I}_R \\ \overline{V}_R &= -j\omega M \overline{I}_T \end{aligned} \tag{2}$$

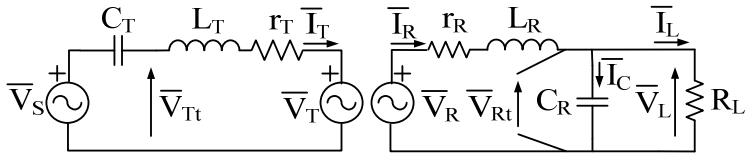

Figure 3. SP resonant topology WBC circuit diagram.

Here, M and ω are the mutual inductance between the coils and the WBC supply angular frequency. Figure 4 shows the phasor diagram for SP resonant topology, where $\overline{V}_T$, $\overline{V}_R$ are shown orthogonal to $\overline{I}_R$ and $\overline{I}_T$, respectively, as given in (2).

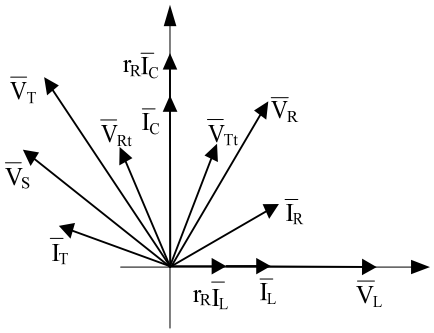

Figure 4. Phasor diagram for SP resonant topology.

It is obvious from Figure 3 that the receiver current $(\overline{I}_R)$ is the phasor sum of the load current $(\overline{I}_L)$ and the current in the receiving resonant capacitor $(\overline{I}_C)$ and is given as

$$\overline{I}_R = \overline{I}_L + \overline{I}_C \tag{3}$$

Since $\overline{I}_L$ and $\overline{V}_L$ are in the same phase, then $\overline{I}_C$ and $\overline{I}_L$ are orthogonal to each other as $\overline{I}_C$ is equal to $j\omega C_R \overline{V}_L$. Replacing $\overline{I}_C$ with $j\omega C_R \overline{V}_L$, in Equation (3), then is represented in (4) as

$$\overline{I}_R = \overline{I}_L + j\omega C_R \overline{V}_L \tag{4}$$

By applying KVL in the Figure 3 receiving-side of the WBC circuit, we get

$$\overline{V}_R = r_R \overline{I}_R + j\omega L_R \overline{I}_R + \overline{V}_L \tag{5}$$

Equation (5) can further be simplified by using (4), which can be represented in Equation (6) as

$$\overline{V}_R = r_R \overline{I}_L + j\, r_R \frac{\overline{V}_L}{\omega L_R} + j\omega L_R \overline{I}_L \tag{6}$$

Rearranging (2) using (6) expressions for $\overline{I}_T$ is obtained as

$$\overline{I}_T = \frac{j r_R \overline{I}_L - r_R \frac{\overline{V}_L}{\omega L_R} - \omega L_R \overline{I}_L}{\omega M} \tag{7}$$

Doing some manipulation in Figure 3 and using (2) and (7), the expression for $\overline{V}_S$ is

$$\overline{V}_S = -\left(\frac{r_T r_R}{\omega^2 M L_R}\overline{V}_L + \frac{r_T L_R}{M}\overline{I}_L + \frac{M}{L_R}\overline{V}_L\right) + j\left(\omega M + \frac{r_T r_R}{\omega M}\right)\overline{I}_L \tag{8}$$

3. FOMs and Their Calculation

3.1. FOMs Introduction

The circuit mentioned in Figure 3 is used to calculate the FOMs. They are calculated under the assumption of neglecting the circuitry losses between the battery and the receiver. Hence, the power absorbed by the battery, denoted by P_B, coincides with the power entering the load resistance. Five FOMs such as overall efficiency η, Power Transfer Ratio (PTR), Receiver Efficiency (RE), Power Source Sizing Factor (PSSF), and Receiver Coil Sizing Factor (RCSF), are considered and are defined as follows:

$$\eta \triangleq \frac{P_B}{P_S} \tag{9}$$

$$PTR \triangleq \frac{P_R}{P_S} \tag{10}$$

$$RE \triangleq \frac{P_B}{P_R} \tag{11}$$

$$PSSF \triangleq \frac{A_S}{P_N} \tag{12}$$

$$RCSF \triangleq \frac{A_R}{P_N} \tag{13}$$

Here, P_S is the power source output power, P_R is the active power transferred to the receiver, A_S is the power source sizing power, and A_R is the sizing power of the receiving coil. Sizing powers A_S and A_R are defined as

$$A_S = max(V_S) * max(I_T) \tag{14}$$

$$A_R = max(V_{Rt}) * max(I_R) \tag{15}$$

where max represents the maximum of the specified quantity in the battery-charging process. It should be noted that PSSF and RCSF are the measures of cost and volume of the WBC system as a function of nominal power absorbed by the battery. Similarly, the detail power-sizing factor of the transmitting coil is expressed in Appendix A.

3.2. FOMs Calculation

Taking into account the first three FOMs from (9) to (11), they can be expressed as

$$\eta = \frac{P_B}{P_{jT} + P_{jR} + P_B} \tag{16}$$

$$PTR = \frac{P_{jR} + P_B}{P_{jT} + P_{jR} + P_B} \tag{17}$$

$$RE = \frac{P_B}{P_{jR} + P_B} \tag{18}$$

where $P_{jT} = r_T I_T^2$ and $P_{jR} = r_R I_R^2$ are the losses associated with the transmitter and receiver and $P_B = R_L I_L^2$. Substituting the respective current in (16)–(18) with (4) and (7) and using the relation $R_L = V_L / I_L$, one can achieve

$$\eta = \frac{1}{\frac{r_T}{(\omega M)^2}\left[\left\{\left(\frac{r_R}{\omega L_R}\right)^2 + \frac{M^2 r_R}{L_R^2 r_T}\right\}R_L + \left\{\frac{(\omega M)^2}{r_T} + 2r_R\right\} + \frac{1}{R_L}\left\{(\omega L_R)^2 + \frac{r_R(\omega M)^2}{r_T} + r_R^2\right\}\right]} \tag{19}$$

$$PTR = \frac{\frac{r_R}{R_L} + \frac{r_R}{(\omega L_R)^2}R_L + 1}{\frac{r_T}{(\omega M)^2}\left[\left\{\left(\frac{r_R}{\omega L_R}\right)^2 + \frac{M^2 r_R}{L_R^2 r_T}\right\}R_L + \left\{\frac{(\omega M)^2}{r_T} + 2r_R\right\} + \frac{1}{R_L}\left\{(\omega L_R)^2 + \frac{r_R(\omega M)^2}{r_T} + r_R^2\right\}\right]} \tag{20}$$

$$E = \frac{1}{\frac{r_R}{R_L} + \frac{r_R}{(\omega L_R)^2}R_L + 1} \tag{21}$$

Maximum RE using (21) is obtained for

$$R_{L,RE\ max} = \omega L_R \tag{22}$$

and it is given by

$$RE_{max} = \frac{1}{\frac{2r_R}{\omega L_R} + 1} \tag{23}$$

Expression (22) states that $R_{L,RE}$ max is not dependent on battery parameters and depends on coil parameters; the same happens for RE_{max}.

PSSF and RCSF can be simplified by neglecting the significance of parasitic resistance in the coils. By simplifying (7) and (8) as

$$I_T = \frac{L_R}{M} I_L \tag{24}$$

$$V_S = \sqrt{\left(\frac{M}{L_R} V_L\right)^2 + (\omega M I_L)^2} \tag{25}$$

PSSF is given as

$$PSSF = \frac{max\left[\sqrt{\left(\frac{M}{L_R}V_L\right)^2 + (\omega M I_L)^2}\right] max\left[\frac{L_R}{M}I_L\right]}{P_N} \tag{26}$$

The voltage across the receiving coil terminals is

$$\overline{V}_{Rt} = -j\omega L_R \overline{I}_R - j\omega M \overline{I}_T \tag{27}$$

Substituting (4) and (7) into (27), it is found that

$$\overline{V}_{Rt} = \omega^2 L_R C_R \overline{V}_L \tag{28}$$

From (4) I_R is

$$I_R = \sqrt{I_L^2 + (\omega C_R V_L)^2} \tag{29}$$

RCSF is expressed as

$$RCSF = \frac{max\left[\omega^2 L_R C_R V_L\right] max\left[\sqrt{I_L^2 + (\omega C_R V_L)^2}\right]}{P_N} \tag{30}$$

3.3. WBC Arrangements #1

The circuitry of WBC arrangement #1 is drawn in Figure 5. Due to the presence of L_{DC}, C_{DC}, and L_F as low-pass filters, the current $\overline{I}_L$ will be a square wave and $\overline{V}_L$ sinusoidal. Direct current through the battery will be its peak value, $\overline{I}_L$, and direct voltage across the battery will coincide with its average value of rectified $\overline{V}_L$.

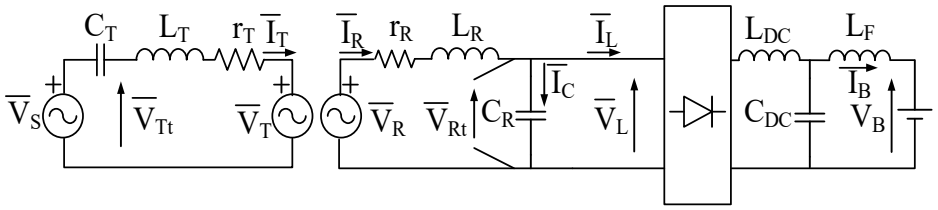

Figure 5. WBC arrangement #1 circuitry.

It is to be noted that $\overline{V}_L$ and $\overline{I}_L$ are in phase, and hence the receiver considers the WBC load as the resistive load. This resistive load, as mentioned previously, is the load resistance and is given as

$$R_L = \frac{V_L}{I_L} \tag{31}$$

The load voltage $\overline{V}_L$ and current $\overline{I}_L$ rms values in terms of V_B and I_B are

$$V_L = \frac{\pi}{2\sqrt{2}} V_B \tag{32}$$

$$I_L = \frac{4}{\pi\sqrt{2}} I_B \tag{33}$$

Substituting (32) and (33) into (29) R_L is obtained as

$$R_L = \frac{\pi^2}{8} R_B \tag{34}$$

Due to the presence of a constant term in (34), it is clear that load resistance is proportional to the battery resistance.

3.4. WBC Arrangements #2

Figure 6 draws the circuitry for WBC arrangement #2. In this arrangement, let the voltage across C_{DC} be at value $V_{DC} \geq V_M$ and kept constant in any charging condition. Then the chopper duty cycle δ is given as

$$\delta = \left(\frac{V_B}{V_{DC}} \right) \tag{35}$$

During CC mode, δ varies from V_{co}/V_{DC} to V_M/V_{DC}, whilst in CV mode, it remains constant and is equal to V_M/V_{DC}. Due to the duty cycle, the resistance seen by the capacitor C_{DC} is

$$R_{DC,B} = \frac{R_B}{\delta^2} \tag{36}$$

Substituting (35) in (36) and replacing R_B in (34) with $R_{DC,B}$ load resistance becomes

$$R_L = \frac{\pi^2 V_{DC}^2}{8} \frac{R_B}{V_B^2} \tag{37}$$

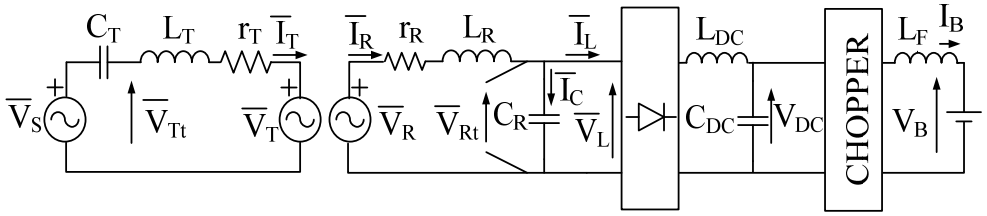

Figure 6. WBC arrangement #2 circuitry.

4. Arrangement Comparison

4.1. Study Case

The study case for this paper is a prototype developed to charge an electric city-car in [23]. Battery and WBC data are listed in Table 1.

Table 1. Battery and WBC system data.

Data	Symbol	Value
Battery voltages	V_{co}, V_M	36, 56 V
Battery currents	I_{CC}, I_{co}	10, 1 A
Battery resistances	R_I, R_N, R_F	3.6, 5.6, 56 Ω
Battery power	P_I, P_N, P_F	360, 560, 56 W
Trans. and rec. coil inductances	L_T, L_R	120 µH
Trans. and rec. coil parasitic resistance	r_T, r_R	0.5 Ω
Trans. and rec. resonant capacitances	C_T, C_R	29 nF
Mutual inductance	M	30 µH
Supply angular frequency	ω	2π·85,000 rad/s

4.2. PTR, RE, and Efficiency

Figures 7–9 plot the PTR, RE, and efficiency with respect to the P_B normalized to P_N. In these plots, curves ABA*C belong to arrangement #1, and curves A*BC belong to arrangement #2. The simulation has been carried out in the MATLAB/Simulink environment. The FOMs expressions are extracted as in (19)–(21), where the value of R_L has been chosen as (34) and (37) for arrangement #1 and arrangement #2, respectively.

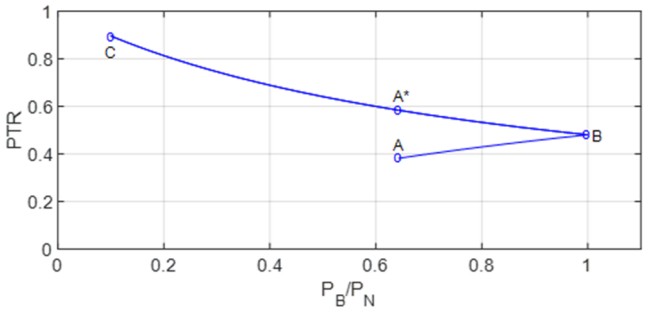

Figure 7. PTR for WBC arrangement #1 and #2.

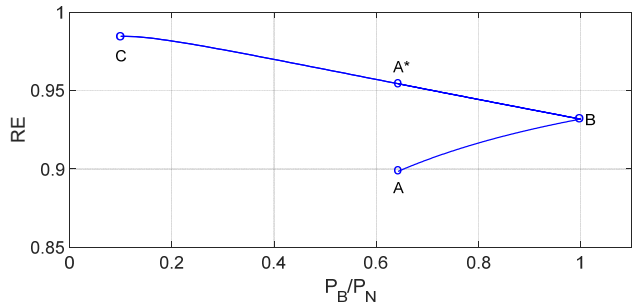

Figure 8. RE for WBC arrangements #1 and #2.

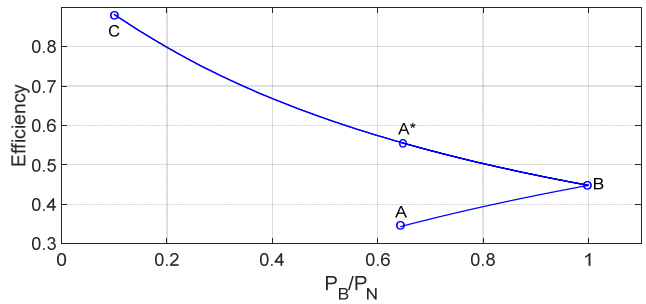

Figure 9. Efficiency for WBC arrangements #1 and #2.

For arrangement #1, load resistance R_L in (19)–(21) is expressed in terms of P_B by substituting (1) into (34), while for arrangement #2, it is done by substituting (1) into (37). Analysis of arrangement #2 is carried out by setting V_{DC} at V_M.

4.3. Arrangement #1

PTR: CC mode starts at P_B = 360 W, where PTR is 0.38, shown as point A in Figure 7. I_T can be assumed to be maximum and constant as (24), and so the constant is the loss associated with it. I_R, as given in (30), increases due to an increase in V_L and so increases losses associated with it. An increase in loss associated with r_R does not account for with respect to an increase in P_B, and hence PTR increases to point B shown in Figure 7.

CV mode starts from P_B = 560 W as point B, as shown in Figure 7. By comparing (24) and (29) and considering the data of Table 1, it is found that I_T is approximately four times greater than that of I_R, and hence loss associated with I_T is much higher than that of I_R. I_T mitigates the impact of I_R, which causes an increase in PTR and reaches a value of 0.89 at point C at the completion of CV mode.

RE: During CC mode, starting from point A shown in Figure 8, and having RE close to 0.9, a small increase in loss associated with r_R (as discussed in the case of PTR) is compensated by the increase in P_B that increases RE to 0.93 at the completion of mode, shown as point B.

In CV mode, starting from point B in Figure 8, RE increases due to the fact that P_B decreases linearly to I_L while losses are associated with I_R with the power of two. RE reaches its maximum at P_B = 60.3 W and starts mitigating onwards due to the influence of I_C over I_L.

Efficiency: During CC mode, as explained for PTR and RE, variation of efficiency, as shown in Figure 8, from points A to B is expected. In CV mode, losses in r_T conquer the losses in r_R due to the fact that I_T is approximately four times that of I_T, and hence the curve of efficiency follows PTR and reaches point C at the completion of CV mode through point A*.

4.4. Arrangement #2

The urge of this arrangement is to have DC link voltage constant during the whole charging process. Thus, charging during CV mode will be the same as arrangement #1 for the same value of DC-link voltage. This, in the case of PTR, RE, and efficiency, will vary from point B to C through A* as in arrangement #1.

During CC mode, P_B increases from P_I to P_N, keeping V_B constant as V_M, and current I_B falls to I_B^* such that

$$I_B^* = \frac{V_{co}}{V_M} I_{CC} \tag{38}$$

and reaches I_{CC} at the completion of CC mode. So, the CC mode for this arrangement will follow the CV mode of arrangement #1, which will move from point A* to point B for PTR, RE, and efficiency.

PTR: During CC mode, variation of PTR as a function of P_B is shown in Figure 7, which starts from point A* at P_B = 360 W and diminishes due to the fact that the effect of r_T losses prevails on the effect of r_R losses as well as an increase in P_B and reaches point B at the completion of CC mode.

RE: CC mode starts from point A' as shown in Figure 8. During CC mode, I_R increases with I_L with its power of two, while the increase in P_B is linear with I_L, so losses associated with r_R overcome the increase in P_B, causing a decrease in RE and reaching point B at the completion of CC mode.

Efficiency: CC mode starts from point A*, as shown in Figure 9. During CC mode, I_R and I_T both increase with I_L with the power of two while the increase in P_B is linear, so losses associated with r_T and r_R prevail on the increase in P_B, causing a decrease in it and reaching point B at the completion of CC mode.

4.5. Efficiency Comparison

Efficiency during CC mode is higher for arrangement #2 because (1) I_T is more or less constant by (24), which in practice is not so and varies slightly due to the presence of r_R, but for simplicity, it can be neglected. For arrangement #1, I_T is maximum, and so are the losses associated with it, but for arrangement #2, I_T starts with I_L, which corresponds to I_B as I_B^* and reaches its maximum where I_B is I_{CC}, and so, loss associated with r_T is always less in this arrangement with reference to arrangement #1, which coincides with the completion of CC mode. (2) In this mode, the effect of the current I_C is very small, so the I_R and losses associated with r_R using the above argument are always greater for arrangement #1 than arrangement #2 and coincide at the completion of CC mode.

4.6. PSSF and RCSF

From (26), it can be observed that PSSF for both arrangements will be maximum at point N on the battery-charging profile. Replacing V_B and I_B with V_M and I_{CC} from (32) and (33) PSSF is calculated as 9.33 and 9.54 if parasitic resistances are considered. The excess PSSF is due to the voltage drop across r_T and r_R.

Expression (30) clarifies that the RCSF for both arrangements will be maximum at point N on the battery-charging profile. Using (32) and (33) and replacing V_B and I_B with V_M and I_{CC}, RCSF is calculated as 1 and remains the same even if parasitic resistance is considered.

5. V_{DC} Effect on the Chopper

In order to select a convenient chopper input voltage V_{DC} for arrangement #2, PTR, RE, and efficiency are investigated for three different values of V_{DC} as V_M, 1.2 V_M, and 1.4 V_M. Figures 10–12 plot the PTR, RE, and efficiency with respect to the P_B normalized to P_N by MATLAB/Simulation.

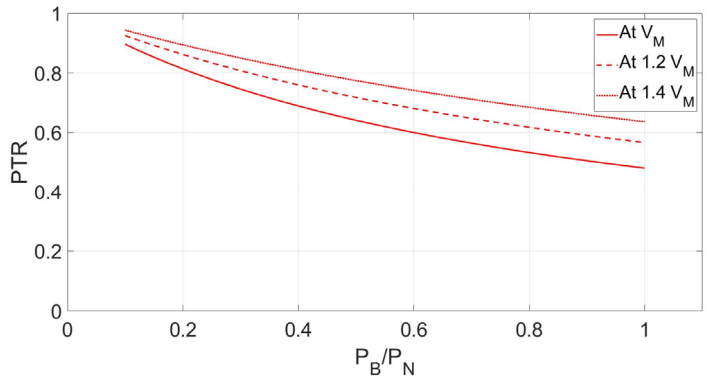

Figure 10. PTR for WBC arrangement #2 with V_{DC} = V_M, 1.2 V_M, and 1.4 V_M.

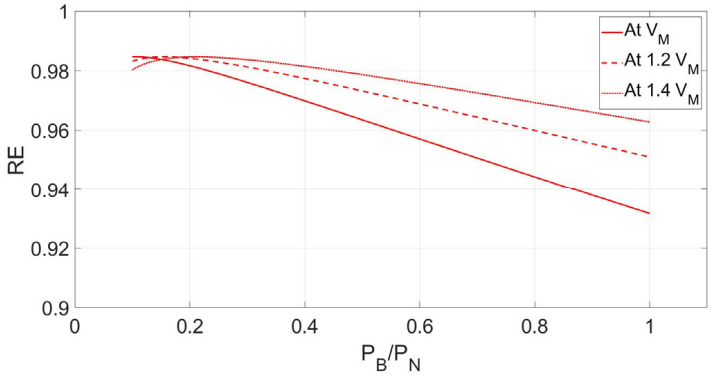

Figure 11. RE for WBC arrangement #2 with V_{DC} = V_M, 1.2 V_M, and 1.4 V_M.

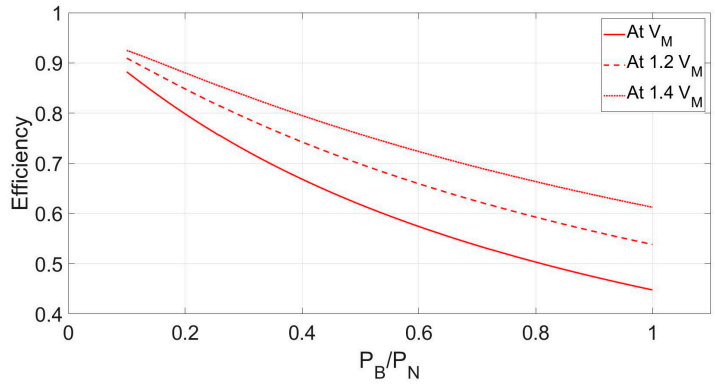

Figure 12. Efficiency for WBC arrangement #2 with V_{DC} = V_M, 1.2 V_M, and 1.4 V_M.

PTR: Figure 10 shows that PTR increases with the higher value of V_M, which is due to the fact that for a given value of P_B, I_L is less for $V_{DC} > V_M$, and so are the values of I_T and I_R. From (24) and (29), it is clear that the decrease in I_T is significantly higher than I_R. Due to this, losses associated with r_T dominate over losses associated with r_R.

RE: Figure 11 shows that for the higher value of P_B, RE increases with V_{DC} because, for a given value of P_B, since V_L is high current I_L is low, and so losses associated with r_R will be less, which results in the increase of RE. For the lower value of P_B, I_C predominates over I_L, which is high for $V_{DC} > V_M$ and causes a decrease in RE.

Efficiency: Figure 12 shows that efficiency increases with the increase of V_{DC} due to the fact that, for the higher value of V_{DC}, current I_L is low, and I_T and I_R will also be lower. For the lower value of I_T and I_R, losses associated with them will be low, which results in an increase in efficiency.

PSSF and RCSF: Using (26) PSSF for $V_{DC} = V_M$, 1.2 V_M and 1.4 V_M are calculated as 9.54, 9.59, and 9.64, respectively, by considering the effect of parasitic resistances. The RCSF from (30) for the same values of V_{DC} is 1, 1.21, and 1.41, respectively.

6. Experimental Analysis

The theoretical finding for efficiency is checked by an experiment executed on SP resonant WBC with the characteristics reported in Table 1. The experimental setup for WBC systems is shown in Figure 13. The variable resistor is used in place of the battery for both arrangements. The first set of tests is carried out by adjusting the voltage of the power source for the operation of arrangement #1. Operation of arrangement #2 has been carried out on V_{DC} as V_M, 1.2 V_M, and 1.4 V_M. The experimental results are plotted in Figures 14 and 15, which perfectly match the theoretical findings.

Figure 14a–c are plots of the PTR, RE, and efficiency with respect to the P_B normalized to P_N. In these results, the blue line represents the simulated results, and the blue dot represents the experiment results, which almost overlap the simulation results. In these plots, curves ABA*C belong to arrangement #1 in both CC and CV modes, and curves A*BC belong to arrangement #2, whose charging during CV mode will be the same as arrangement #1 for the constant value of DC-link voltage during the whole charging process. This, in the case of PTR, RE, and efficiency, will vary from point B to point C through A* as in arrangement #1. While in the case of the CC mode of arrangement #2 the PTR, RE, and efficiency, will vary from point A* to point B. P_B increases from P_I to P_N keeping V_B constant as V_M, current I_B falls to I_B^* and reaches I_{CC} at the completion of CC mode.

Figure 15a–c are plots of the PTR, RE, and efficiency with respect to the P_B normalized to P_N. In these results, the red line represents the simulated results, and the blue dot represents the experiment results. Those are almost identical to simulation results. To select a convenient chopper input voltage V_{DC} for arrangement #2 PTR, RE and efficiency are investigated for three different values of V_{DC} as V_M, 1.2 V_M, and 1.4 V_M. It is found that, the PTR, RE, and efficiency increase with a higher value of V_M, which is due to the fact that for a given value of P_B, I_L is less for $V_{DC} > V_M$.

The components of the two different arrangements of the WBC are quite similar. These components are purchased from retailers in a very small number of samples or have been designed and manufactured on purpose; consequently, the price of the prototype is much higher than that of a mass-produced system. The total cost for the prototype in arrangement #1 was equal to EUR 5800, as mentioned in [26,27]. However, WBC arrangement #2 is a bit more expensive than WBC arrangement #1, as arrangement #2 has an extra set of DC-DC converters and a respective controller to regulate the current for battery charging.

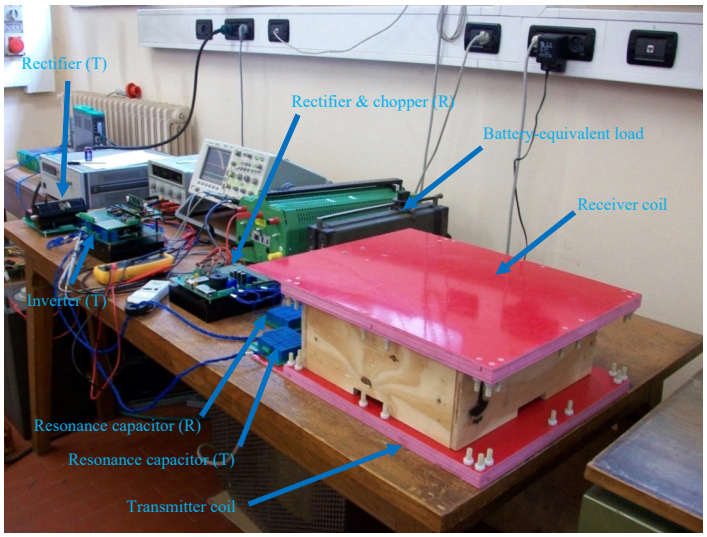

Figure 13. WBC prototype.

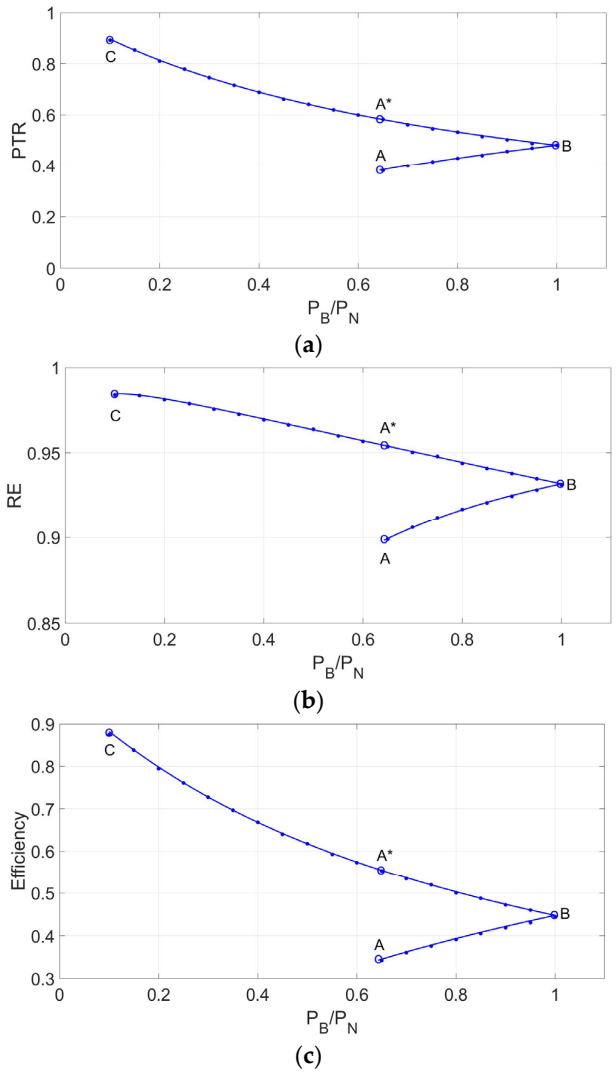

Figure 14. Experimental results for (**a**) PTR, (**b**) RE, and (**c**) efficiency for WBC arrangements #1 and #2.

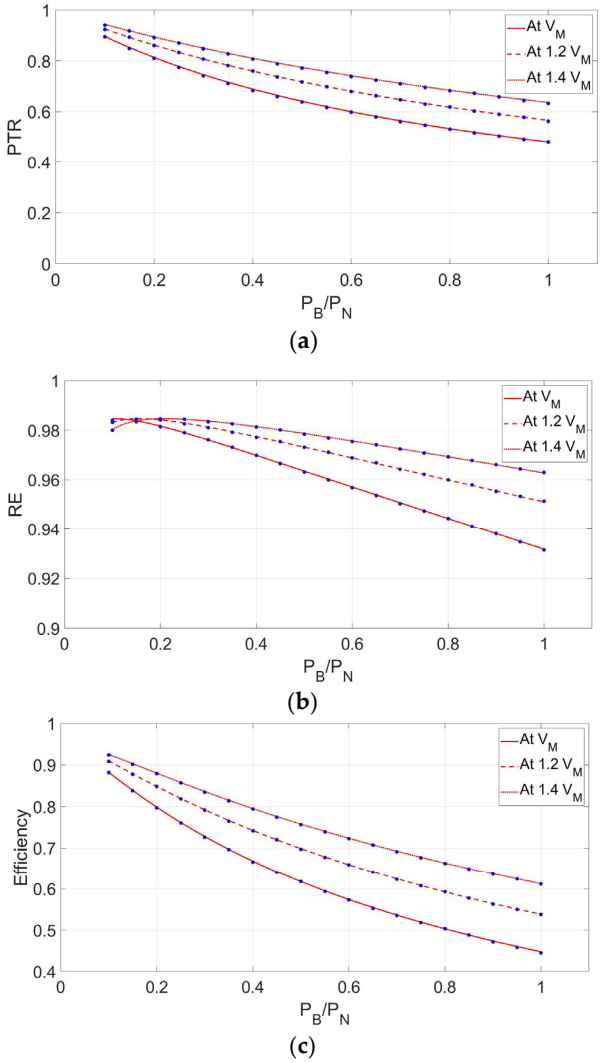

Figure 15. Experimental results for (**a**) PTR, (**b**) RE, and (**c**) efficiency for WBC arrangement #2 with VDC = VM, 1.2 VM, and 1.4 VM.

7. Conclusions

The paper deals with two different arrangements for WBC. The first charging arrangement charges the battery without using a chopper and controls rectifier voltage/current based on the battery-charging profile, while the second charging arrangement charges the battery with the chopper. Based on their performance on five FOMs as measured by efficiency, PTR, RE, PSSF, and RCSF, the second arrangement is found to be more favorable for WBC. To select the most convenient chopper input voltage, three different voltages were considered, with a higher value of the chopper input voltage found to be most suitable for WBC, apart from a small compromise with PSSF and RCSF. However, in terms of cost estimation, arrangement #2 is costly compared to arrangement #1.

Author Contributions: Conceptualization, A.K., R.K.J. and M.B.; methodology A.K., R.K.J. and M.B.; software, A.K. and R.K.J.; validation, A.K. and R.K.J.; formal analysis, A.K. and R.K.J.; investigation, A.K. and R.K.J.; resources A.K., R.K.J., M.B., C.B.K., S.J. and G.M.; data curation, A.K., R.K.J., M.B., C.B.K., S.J., G.M. and A.S.; writing—original draft preparation, A.K., R.K.J., M.B., C.B.K., S.J., G.M. and A.S.; writing—review and editing, A.K., R.K.J., M.B., C.B.K., S.J., G.M. and A.S.; visualization, A.K., R.K.J., M.B., C.B.K., S.J., G.M. and A.S.; supervision, A.K., R.K.J. and M.B. All authors have read and agreed to the published version of the manuscript.

Funding: This research received no external funding.

Data Availability Statement: Most of the data and the results are reported in the paper. Additional data can be requested from the corresponding author.

Conflicts of Interest: The authors declare no conflict of interest.

Nomenclature

WBCSs	Wireless Battery Charging Systems
PFC	Power Factor Correction
HFI	High-Frequency Inverter
CN	Compensation Network
EV	Electrical Vehicle
SS	Series–Series
SP	Series–Parallel
FOM	Figure of Merit
CC	Constant Current
CV	Constant Voltage
I_B	Battery Current
V_B	Battery Voltage
R_B	Battery resistance
P_B	Battery power
I_{co}	Cutoff current
V_{co}	Cutoff voltage
I_{CC}	Normalized current in CC mode
V_M	Normalized maximum voltage of battery
R_N	Normalized resistance at point N
P_N	Normalized power at point N
$\overline{V}_S$	Power source voltage
$\overline{I}_T$	Transmitter-side current
$\overline{I}_R$	Receiver-side current
C_T	Transmitter-side resonant capacitor
C_R	Receiver-side resonant capacitor
$\overline{V}_{Tt}$	Transmitter coil terminal voltage
$\overline{V}_{Rt}$	Receiver coil terminal voltage
r_T	Transmitter coil parasitic resistance
r_R	Receiver coil parasitic resistance
$\overline{V}_T$	Transmitter coil induce voltage
$\overline{V}_R$	Receiver coil induce voltage
$\overline{I}_C$	Receiver-side capacitor current
$\overline{I}_L$	Load current
R_L	Load resistance
$\overline{V}_L$	Voltage across R_L
M	Mutual inductance
ω	Supply angular frequency
η	Efficiency
PTR	Power Transfer Ratio
RE	Receiver Efficiency
PSSF	Power Source Sizing Factor
RCSF	Receiver Coil Sizing Factor
P_S	Power source output power
P_R	Power transfer to receiver
A_S	Power source sizing power
A_R	Receiver coil sizing power
P_{jT}	Loss of transmitter coil
P_{jR}	Loss of receiver coil
L_{DC}	Low pass filter inductor
C_{DC}	Low pass filter capacitor
V_{DC}	Voltage across C_{DC} in arrangement #2
δ	Chopper duty cycle

Appendix A

The power-sizing factor of the receiving coil is given by (15), where $max(V_{Rt})$ is the maximum of (28). Similarly, the power-sizing factor of the transmitting coil is expressed as

$$A_T = max(V_{Tt}) * max(I_T) \tag{A1}$$

From the circuit diagram of Figure 3, the voltage across the transmitting coil terminals is

$$\overline{V}_{Tt} = \overline{V}_T + j\omega L_T \overline{I}_T \tag{A2}$$

Using (2), (4), and (7) rms values of $\overline{V}_{Tt}$ is given as

$$V_{Tt} = \left[\left(\omega^2 M C_R V_L \right)^2 + I_L^2 \left(\frac{\omega M^2 - \omega L_T L_R}{M} \right)^2 \right]^{\frac{1}{2}} \tag{A3}$$

The maximum of V_{Tt} is again achieved at point N of the charging profile, where both I_R and I_T get the maximum values. Using (A1), (A2), (24), and (15), (28), (29), the relationship between A_T and A_R can be written for point N as

$$A_T = \frac{8}{M\pi^2\omega^2} \frac{\left[\left(\frac{\omega^2 M C_R \pi}{2\sqrt{2}} \right)^2 + \left(\frac{\omega M^2 - \omega L_T L_R}{M} \right)^2 \left(\frac{4}{\pi\sqrt{2}} \right)^2 \frac{1}{R_N^2} \right]^{\frac{1}{2}}}{\left[\left(\frac{4}{\pi\sqrt{2}} \right)^2 + \left(\frac{\omega C_R \pi}{2\sqrt{2}} \right)^2 R_N^2 \right]^{\frac{1}{2}}} A_R \tag{A4}$$

Equation (A4) shows that the relationship between the sizing factors of the transmitting and receiving coils depend on the inductive parameters of the coils, receiving a stage capacitor and battery resistance at point N.

References

1. Kumar, A.; Singh, A.R.; Meena, N.K.; Deng, Y.; He, X.; Kumar, P.; Bansal, R.C. Design and Evaluation of Microgrids Based on Renewable Energy Technologies with a Perspective of Sustainable Development. *Bansal Handb. Renew. Energy Technol. Syst.* **2021**, 385–415. [CrossRef]
2. Rangu, S.K.; Lolla, P.R.; Dhenuvakonda, K.R.; Singh, A.R. Recent trends in power management strategies for optimal operation of distributed energy resources in microgrids: A comprehensive review. *Int. J. Energy Res.* **2020**, *44*, 9889–9911. [CrossRef]
3. Vázquez-Leal, H.; Gallardo-Del-Angel, A.; Castañeda-Sheissa, R.; González-Martínez, F.J. The phenomenon of wireless energy transfer: Experiment and philosophy. In *Wireless Power Transfer—Principles and Engineering Explorations*; Kim, K.Y., Ed.; IntechOpen: London, UK, 2012.
4. Bertoluzzo, M.; Mude, K.N.; Buja, G. Preliminary investigation on contactless energy transfer for electric vehicle battery recharging. In Proceedings of the 2012 IEEE 7th International Conference on Industrial and Information Systems (ICIIS), Madras, India, 6–9 August 2012; pp. 1–6.
5. Buja, G.; Jha, R.K.; Bertoluzzo, M.; Naik, M.K. Analysis and comparison of two wireless battery charger arrangements for electric vehicles. *Chin. J. Electr. Eng.* **2015**, *1*, 50–57.
6. Tuttle, D.P.; Baldick, R. The evolution of plug-in electric vehicle grid interactions. *IEEE Trans. Smart Grid* **2012**, *3*, 500–505. [CrossRef]
7. Kaneko, Y.; Abe, S. Technology trends of wireless power transfer systems for electric vehicle and plug-in hybrid electric vehicle. In Proceedings of the 2013 IEEE 10th International Conference on Power Electronics and Drive Systems (PEDS), Kitakyushu, Japan, 22–25 April 2013; pp. 1009–1014.
8. Mude, K.N.; Bertoluzzo, M.; Buja, G. Design of contactless battery charger for electric vehicle. In Proceedings of the African Electrical Technology Conference, Pamplemousses, Mauritius, 12–15 May 2013; pp. 1099–1104.
9. Zhou, W.; Ma, H. Design considerations of compensation topologies in ICPT system. In Proceedings of the APEC 07-Twenty-Second Annual IEEE Applied Power Electronics Conference and Exposition, Anaheim, CA, USA, 25 February–1 March 2007; pp. 985–990.
10. Zhang, W.; Wong, S.-C.; Tse, C.K.; Chen, Q. Analysis and comparison of secondary series- and parallel-compensated inductive power transfer systems operating for optimal efficiency and load-independent voltage-transfer ratio. *IEEE Trans. Power Electron.* **2014**, *29*, 2979–2990. [CrossRef]

11. Bertoluzzo, M.; Buja, G.; Mude, K.N. Characteristic Evaluation of Wireless Battery Chargers for Electric Vehicles. *Electromotion* **2013**, *20*, 103–108.
12. Li, W.; Zhao, H.; Li, S.; Deng, J.; Kan, T.; Mi, C.C. Integrated LCC Compensation Topology for Wireless Charger in Electric and Plug-in Electric Vehicles. *IEEE Trans. Ind. Electron.* **2015**, *62*, 4215–4225. [CrossRef]
13. Pantic, Z.; Bhattacharya, S.; Lukic, S. Optimal resonant tank design considerations for primary track compensation in inductive power transfer systems. In Proceedings of the IEEE Energy Conversion Congress and Exposition (ECCE), Atlanta, GA, USA, 2-16 September 2010; pp. 1602–1609.
14. Bailian, N.; Chung, C.Y.; Chan, H.L. Design and comparison of parallel and series resonant topology in wireless power transfer. In Proceedings of the IEEE (ICIEA), Melbourne, Australia, 19–21 June 2013; pp. 1832–1837.
15. Pantic, Z.; Lukic, S. Framework and topology for active tuning of parallel compensated receivers in wireless power transfer systems. *IEEE Trans. Power Electron.* **2012**, *99*, 1–10.
16. Kumar, A.; Bertoluzzo, M.; Jha, R.K.; Sagar, A. Analysis of Losses in Two Different Control Approaches for S-S Wireless Power Transfer Systems for Electric Vehicle. *Energies* **2023**, *16*, 1795. [CrossRef]
17. Keeling, N.A.; Covic, G.A.; Boys, J.T. A Unity-Power-Factor IPT Pickup for High-Power Applications. *IEEE Trans. Ind. Electron.* **2010**, *57*, 744–751. [CrossRef]
18. Chao, Y.-H.; Shieh, J.-J.; Pan, C.-T.; Shen, W.-C.; Chen, M.-P. A Primary-Side Control Strategy for Series-Parallel Loosely Coupled Inductive Power Transfer Systems. In Proceedings of the IEEE Conference on Industrial Electronics and Applications (ICIEA), Harbin, China, 23–25 May 2007; pp. 2322–2327.
19. Chen, J.; Maksimovic, D.; Erickson, R. Buck-boost PWM converters having two independently controlled switches. In Proceedings of the IEEE Power Electronics Specialists Conference (PESC), Vancouver, BC, Canada, 17–21 June 2001; Volume 2, pp. 736–741.
20. Yao, C.; Ruan, X.; Cao, W.; Chen, P. A Two-Mode Control Scheme with Input Voltage Feed-Forward for the Two-Switch Buck-Boost DC–DC Converter. *IEEE Trans. Power Electron.* **2014**, *29*, 2037–2048. [CrossRef]
21. Colak, K.; Bojarski, M.; Asa, E.; Czarkowski, D. A constant resistance analysis and control of cascaded buck and boost converter for wireless EV chargers. In Proceedings of the IEEE Applied Power Electronics Conference and Exposition (APEC), Charlotte, NC, USA, 15–19 March 2015; pp. 3157–3161.
22. Wu, H.H.; Covic, G.A.; Boys, J.T.; Hu, A.P. A 1 kW inductive charging system using AC processing pickups. In Proceedings of the IEEE Industrial Electronics and Applications (ICIEA), Beijing, China, 21–23 June 2011; pp. 1999–2004.
23. Sagar, A.; Kumar, A.; Bertoluzzo, M.; Jha, R.K. Analysis and Design of a Two-winding Wireless Power Transfer System with Higher System Efficiency and Maximum Load Power. In Proceedings of the IECON 2022—48th Annual Conference of the IEEE Industrial Electronics Society, Brussels, Belgium, 18–21 October 2022; pp. 1–6.
24. Sagar, A.; Bertoluzzo, M.; Kumar, A. Analysis and Comprehensive Comparison of Wireless Power Transfer System Using SS and SP topology for Electric Vehicle Charging. In Proceedings of the 2023 International Conference on Computational Intelligence, Communication Technology and Networking (CICTN), Ghaziabad, India, 20–21 April 2023; pp. 235–240.
25. Haller, S.; Alam, M.F.; Bertilsson, K. Reconfigurable Battery for Charging 48 V EVs in High-Voltage Infrastructure. *Electronics* **2022**, *11*, 353. [CrossRef]
26. Buja, G.; Bertoluzzo, M.; Mude, K.N. Design and Experimentation of WPT Charger for Electric City-Car. *IEEE Trans. Ind. Electron.* **2015**, *62*, 7436–7447. [CrossRef]
27. Bertoluzzo, M.; Giacomuzzi, S.; Kumar, A. Design of a Bidirectional Wireless Power Transfer System for Vehicle-to-Home Applications. *Vehicles* **2021**, *3*, 406–425. [CrossRef]